CCS Chemistry

RESEARCH ARTICLE

Received: Mar. 20, 2022 | Accepted: Apr. 18, 2022 | Published: May 24, 2022

Pressure-Induced Intermetallic Charge Transfer and Semiconductor-Metal Transition in Two-Dimensional $AgRuO_3$

Chuanhui Zhu[1], Jinjin Yang[1], Pengfei Shan[2], Mei-Huan Zhao[1], Shuang Zhao[1], Cuiying Pei[3], Bowen Zhang[4], Zheng Deng[2], Mark Croft[5], Yanpeng Qi[3,6,7], Lihong Yang[2], Yonggang Wang[8], Xiaojun Kuang[4], Long Jiang[1], Dao-Xin Yao[9], Jin-Guang Cheng[2]* & Man-Rong Li[1]*

[1]Key Laboratory of Bioinorganic and Synthetic Chemistry of Ministry of Education, School of Chemistry, Sun Yat-sen University, Guangzhou 510275, [2]Beijing National Laboratory for Condensed Matter Physics, Institute of Physics, Chinese Academy of Sciences, Beijing 100190, [3]School of Physical Science and Technology, ShanghaiTech University, Shanghai 201210, [4]College of Chemistry and Bioengineering, Guilin University of Technology, Guilin 541004, [5]Department of Physics and Astronomy, Rutgers, The State University of New Jersey, Piscataway, NJ 08854, [6]ShanghaiTech Laboratory for Topological Physics, ShanghaiTech University, Shanghai 201210, [7]Shanghai Key Laboratory of High-Resolution Electron Microscopy, ShanghaiTech University, Shanghai 201210, [8]Center for High Pressure Science and Technology Advanced Research (HPSTAR), Beijing 100094, [9]Guangdong Key Laboratory of Magnetoelectric Physics and Devices, School of Physics, Sun Yat-sen University, Guangzhou 510275

**Corresponding authors:* jgcheng@iphy.ac.cn; limanrong@mail.sysu.edu.cn

Cite this: *CCS Chem.* **2022**, Just Published. DOI: 10.31635/ccschem.022.202201989

The intricate correlation between charge degrees of freedom and physical properties is a fascinating area of research in solid state chemistry and condensed matter physics. Herein, we report on the pressure-induced successive charge transfer and accompanied resistive evolution in honeycomb layered ruthenate $AgRuO_3$. Structural revisiting and spectroscopic analyses affirm the ilmenite type *R*-3 structure with mixed valence cations as $Ag^{+1/+2}Ru^{+4/+5}O_3$ at ambient pressure. In-situ pressure- and temperature-dependent resistance variation reveals a successive insulator-metal-insulator transition upon pressing, accompanied by unprecedented charge transfer between Ag and Ru under applied pressure, and a further structural phase transition in the insulator region at higher pressure. These phenomena are also corroborated by in-situ pressure-dependent Raman spectra, synchrotron X-ray diffraction, bond valence sums, and electronic structure calculations, emphasizing the dominated rare Ag^{2+}, and near zero thermal expansion in the *ab*-plane in the metallic zone mostly due to the Jahn-Teller effect of d^9-Ag^{2+}. The multiple electronic instabilities in $AgRuO_3$ may offer new possibilities toward novel and unconventionally physical and chemical behaviors in strongly correlated honeycomb lattices.

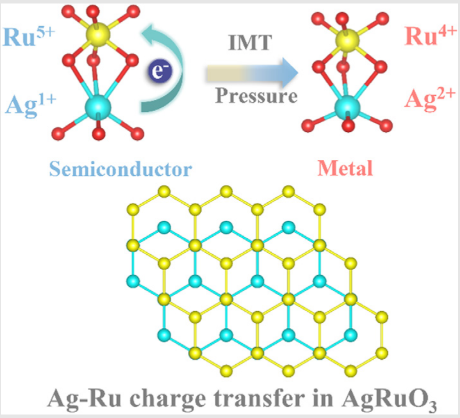

Keywords: intermetallic charge transfer, semiconductor-metal transition, honeycomb layered ruthenates, high pressure

Citation: *CCS Chem.* **2022**, Just Published. DOI: 10.31635/ccschem.022.202201989
Link to VoR: https://doi.org/10.31635/ccschem.022.202201989

Introduction

Pressure-induced crystal and electronic structural transition of solids have proven a treasure trove for solid-state chemistry, condensed matter physics, and material science.[1-3] In particular, for transition metal oxides with strong interplays between lattice, charge, spin, and orbital, pressure has demonstrated significant influence on the exotic phenomena in correlated systems, including magnetoelectric multiferroics, colossal magnetoresistance, and high temperature superconductivity.[4-6] The perovskite $BiNiO_3$ and ilmenite $FeTiO_3$ are two typical compounds that exhibit pressure-induced intermetallic charge transfer.[7,8] The electronic configurations between two metallic ions can be altered simultaneously via intermetallic charge transfer, giving rise to drastic changes in structure and physical properties.[9-11] For instance, $RCu_3Fe_4O_{12}$ (R = rare earth or Bi) displays an intermetallic charge transfer accompanied with paramagnetism-to-antiferromagnetism transitions, negative thermal expansion (NTE), and above room-temperature metal-to-insulator transition (MIT) as well.[12-14] Mixed valence arising from intermetallic charge transfer has also been observed in 4*d*/5*d* oxides, such as in pressure-induced hexagonal perovskite $Ba_3BiM_2O_9$ (M = Ru, Ir) and delafossite Cu_2IrO_3, reflecting the spatial dispersion of *d* orbitals.[15,16]

As one of the most appealing quantum materials, low-dimensional ruthenates have received growing attention due to their unique physical properties and quantum critical phenomena as reported in quasi-two-dimensional (2D) Ruddlesden-Popper phase, $PbSb_2O_6$-type analog, delafossite derivative, and halogenide.[17,18] Particularly, honeycomb-layered ruthenates, which resemble the so-called Kitaev model with strong geometric frustration, are extremely interesting.[19] The $PbSb_2O_6$-type $SrRu_2O_6$ shows high antiferromagnetic (AFM) ordering up to 565 K originated from the strong exchange interactions and large magnon gap.[20,21] In delafossite derivatives, dimerized Li_2RuO_3 is a valence bond liquid with spin-singlet ground state and $Cu_3LiRu_2O_6$ demonstrates pressure-induced nonmetallic-metal to bad-metal transition.[22-24] α-$RuCl_3$ is a hotspot in 2D ruthenates, because it demonstrates very strong exchange anisotropy and is a promising candidate for Kitaev quantum spin liquid, which is usually expected in a frustrated 2D system with $S = 1/2$ ions, such as d^5-Ru^{3+} and d^9-Ni^+, Cu^{2+}, and Ag^{2+}.[25-29] Recently, $AgRuO_3$, which adopts an exotic perovskite-related ilmenite structure (R-3c), was reported to show an AFM transition around 342 K with semiconducting behavior.[30,31] The honeycomb-layered RuO_6 sheets are effectively separated by the larger size Ag ions, which, when compared with other conventional ilmenites, increases the interlayer distance, and renders strengthened 2D features in $AgRuO_3$. However, the structure and physical properties of $AgRuO_3$ under high-pressure (HP) remain unknown and worthy of further exploration.

In this work, we revisited the crystal structure of $AgRuO_3$ over a wide temperature range, and plotted the temperature- and pressure-dependent resistance phase diagram to understand this emerging compound in more depth. By combining various diffraction and spectroscopic techniques, we show that the ambient pressure (AP) $AgRuO_3$ belongs to the R-3 space group with the charge formula as $Ag^{+1/+2}Ru^{+4/+5}O_3$, instead of the reported R-3c. Upon pressurization, a successive insulator-metal-insulator and structural transition is ignited in the honeycomb lattice. Comprehensive experimental and theoretical structure investigations reveal a simultaneous charge transfer between Ag and Ru under applied pressure, accompanied with insulator-metal transition (IMT) at the Ag^{2+}-dominated area. Further structural transitions to $P2/m$ at higher pressure are also predicted.

Experimental Methods

Synthesis

Samples of $AgRuO_3$ were prepared via hydrothermal reaction in a Teflon-lined stainless steel autoclave following a literature report.[31] A mixture of Ag_2O (99.9%, Aladdin) and excess $KRuO_4$ (98%, Strem) at a molar ratio of 1:2.1 was added into distilled water (8 mL) and sonicated for 20 min. Subsequently, the mixture was sealed in a 25 mL Teflon-lined steel autoclave and heated at 423 K (heating rate of 5 K/min) for 24–72 h, and then cooled (cooling rate between 10 K/day and natural cooling) to room temperature. Optimal conditions were found by heating 72 h before natural cooling. The obtained samples were washed with deionized water and then ethanol before being dried at 323 K for 30 min. Finally, black crystals were obtained.

Chemical and crystal structure characterizations

The sample was initially characterized by single-crystal X-ray diffraction (SCXRD, SuperNova, $Mo_{K\alpha}$ radiation, λ = 0.71073 Å) at 150 K and 293 K. Further in-situ variable-temperature SCXRD data were collected from 100 K to 293 K (Bruker D8 Adventure Photon III (Guangzhou, Guangdong, China), $GaIn_{K\alpha}$ radiation, λ = 1.34138 Å). Powder XRD (PXRD) patterns were also recorded using a Rigaku (DMAX 2200 VPC) (Guangzhou, Guangdong, China) instrument equipped with $Cu_{K\alpha}$ radiation (λ = 1.5418 Å) for phase determination. In-situ variable-temperature PXRD (VT-PXRD) data were collected from 4 to 293 K (SmartLab, $Cu_{K\alpha}$, λ = 1.5418 Å). Room-temperature synchrotron powder XRD (SPXRD) data were collected at ambient and high pressures on beamline BL14B (λ = 0.68840 Å) and BL15U1 (λ = 0.6199 Å), respectively,

Citation: *CCS Chem.* **2022**, Just Published. DOI: 10.31635/ccschem.022.202201989
Link to VoR: https://doi.org/10.31635/ccschem.022.202201989

at the Shanghai Synchrotron Radiation Facility (SSRF). A symmetric diamond anvil cell (DAC) with culet sizes of 250 μm and a Re gasket was used. Silicon oil was used as pressure transmitting media (PTM), and the pressure was determined by the ruby luminescence method. 2D diffraction images were analyzed using FIT2D software. Refinements of the SPXRD and single-crystal diffraction data were performed using programs of Topas Academic V6 and Olex2 (1.2), respectively.[32,33] Thermogravimetric analysis (TGA) was carried out using an NETZSCH TG 209F1 Libra analyzer (Guangzhou, Guangdong, China). Two copies of crystals with a mass of 4.89 mg were placed into two alumina crucibles and heated at a rate of 10 K min^{-1} to 1173 K in Ar atmosphere.

Physical properties and spectroscopic measurements

The magnetic properties were measured on a Magnetic Property Measurement System (MPMS3) over a temperature range of 3 and 380 K. The susceptibility was evaluated in both zero-field-cooled (ZFC) and field-cooled (FC) modes under applied fields of 0.1, 1, and 7 T. The specific heat was measured with a two-tau relaxation method in a Physical Property Measurement System (PPMS-9T). The temperature-dependent resistance of $AgRuO_3$ under different pressures was measured using a DAC made of BeCu alloy ranging from 2.6 to 36.3 GPa. The diameter of the diamond culet was 300 μm. The composite gasket consists of rhenium and insulating *c*-BN, where KBr used as a PTM was loaded into the sample chamber (~100 μm), in which a $AgRuO_3$ sample with dimensions of ~90 μm × 30 μm × 20 μm and a ruby chip were placed. Four pieces of thin platinum were utilized as electrical contacts. The pressure was calibrated at room temperature using the ruby fluorescent method. Temperature dependent resistance measurements in DAC were performed in a liquid-helium cryostat. The X-ray absorption near edge spectroscopy (XANES) data were collected in the total electron yield mode at the Brookhaven National Synchrotron Light Source (NSLS-II) on beamline 7-ID SSA-2 using a Si (111) double crystal monochromators. In situ variable pressure Raman experiments were performed on crystals using a Linkam THMS350V with an excitation wavelength of 532 nm. High pressure was generated using a DAC ranging from 1.07 to 20.20 GPa.

Theoretical calculations

We have explored the crystal structures of $AgRuO_3$ by employing a particle swarm optimization algorithm as implemented in the CALYPSO code in conjunction with first-principles density functional theory (DFT) total-energy calculations.[34–36] Based on the projector augmented-wave method, DFT was implemented in the Vienna Ab Initio Simulation Package.[37–39] The plane wave cut-off energy and *k*-point were 700 eV and 9 × 9 × 9 for geometry optimization and static electronic calculations, respectively. The convergence factor was set as the difference in total energy within 1.0×10^{-7} eV per atom. All atomic positions were fully relaxed until the remaining force on each atom was less than 1.0×10^{-2} eV·Å^{-1}. The exchange correlation energy was treated by the generalized gradient approximation Perdew–Burke–Ernzerhof (GGA-PBE).[40] Electron-electron Coulomb repulsion interactions (*U*) for Ru 4*d* orbitals were considered in the rotationally invariant form (GGA+U) with U_{eff} = 2.0 eV as used to predict semiconducting behavior of $AgRuO_3$.[31,41]

Results and Discussion

Revisiting the crystal and electronic structures and magnetism at AP

Thermal stability of the as-made $AgRuO_3$ was examined by TGA analysis (Supporting Information Figure S1), which shows that $AgRuO_3$ is stable up to around 400 °C in Ar before decomposing into a mixture of Ag and RuO_2 (Supporting Information Figure S1b). The observed weight loss of 6.31% is in reasonable agreement with the expected value of 6.23% due to oxygen release. The crystal structure of $AgRuO_3$ at room temperature was determined by SCXRD, which yielded a rhombohedral *R*-3 rather than the previously reported *R*-3*c* (Supporting Information Table S1) at the experimental conditions.[31] At 100 K, the unit-cell volume (381.70(3) Å^3) is almost identical to that at room temperature (381.75(4) Å^3) as shown in Supporting Information Table S1, owing to the slight expansion (0.005 Å) in the *ab*-plane and contraction (0.031 Å) along the *c*-axis upon cooling. The unit-cell parameters extracted from in situ variable temperature SCXRD reveal that $AgRuO_3$ undergoes a steep NTE in the *ab*-plane and a soft positive thermal expansion along the *c*-axis, rendering a slight overall cell contraction between 100 K and 293 K. This phenomenon can also be observed in Supporting Information Figure S2, where no additional structural transition appears down to 4 K. The anomalous thermal expansion could be responsible for the weak phase transition or the crossover between 125 and 200 K reported in literature.[30] The *R*-3 $AgRuO_3$ adopts the typical ilmenite structure (Figures 1a and 1b, Supporting Information Figure S3, and Tables S1 and S2) with alternative RuO_6 and AgO_6 honeycomb layers in the *ab*-plane, where the face-shared AgO_6 and RuO_6 octahedral pair along the *c*-axis are obstructed by octahedral vacancies. The refined cell dimension (Figure 1b, *R*-3, *a* = 5.2251(6) Å) in the *ab*-plane is similar to that in the literature (Figure 1c, *R*-3c, *a* = 5.2261(6) Å), while the unit cell along the *c*-axis (*c* = 16.0580(1) Å) is about half of the reported value (*c* = 32.358(5) Å). The obtained contractible structure is reproducible on single

Citation: *CCS Chem.* **2022**, Just Published. DOI: 10.31635/ccschem.022.202201989
Link to VoR: https://doi.org/10.31635/ccschem.022.202201989

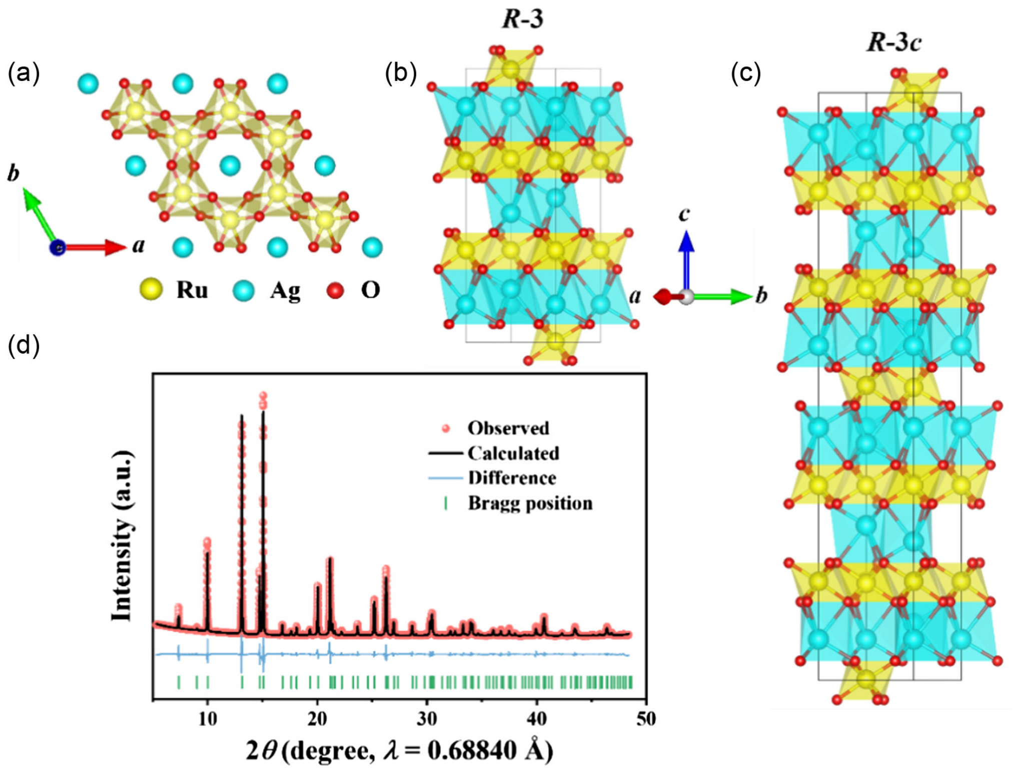

Figure 1 | *Crystal structure determination of $AgRuO_3$. (a) The edge-sharing RuO_6-honeycomb layer motif in the ab-plane projected along the [001] direction. (b) The polyhedral unit cell structure in* R-3 *symmetry in this work. (c) The reported supercell polyhedral unit cell structure in* R-3c *for comparison. (d) Le Bail fit of the SPXRD data in* R-3 *symmetry in this work.*

crystals from different batches, which were measured on different diffractometers with either Ga-In or Mo X-ray targets (Supporting Information Tables S1 and S2), so the possibility of defect-induced uncertainty of structural determination can be ruled out by both SCXRD and PXRD measurements (Supporting Information Figure S4). High resolution SPXRD data fittings (Figure 1d, R-3, $a = 5.2412(2)$, $c = 16.0700(6)$, $V = 382.31(3)$, $R_p/R_{wp} = 6.37/9.18\%$), which, to a great extent, are more reliable than the single-crystal diffraction way, further corroborating the validity of our *R*-3 structure. First-principles calculations are expected to distinguish between the more energetically stable structure between *R*-3 and *R*-3*c*. According to the ground state of $AgRuO_3$ with AFM1 and semiconducting behavior, we further calculated the corresponding energy of different ground states (Supporting Information Table S3). Electron-electron Coulomb repulsion interactions (U) for Ru 4*d* orbitals were considered in the rotationally invariant form (GGA+U) with U_{eff} = 2.0 eV as used to predict the semiconducting behavior of $AgRuO_3$.[31] Based on the AFM1 ground state, *R*-3 demonstrated lower energy than that of *R*-3*c* (35 meV), indicating that the *R*-3 of $AgRuO_3$ seems more stable. Combined with the experimental results, we can further conclude that $AgRuO_3$ belongs to the *R*-3 space group at AP.

Monovalent Ag^+ with a simple closed shell (d^{10}) is the dominant oxidation state of silver. Compounds containing higher oxidation states of Ag are interesting but rare. Ag^{2+} (d^9) in the fluoride was found to be stabilized by the most electronegative F element. In contrast, cuprate-resembling Ag^{2+} oxides are very rare beyond binary systems. $AgBO_3$ (B = Nb, Ta, Sb, Bi), $AgNbO_3$ (*Cmcm*, *Pbcm*, and *Pm*-3*m*), and $AgTaO_3$ (*R*3*cH* and *R*-3*mH*) adopt perovskite-related or $LiNbO_3$-type structures and span a range of different coordination environments from 6 to 12, while $AgSbO_3$ (*R*-3*H*) and $AgBiO_3$ (*R*-3*H*) take analogous structures with $AgRuO_3$.[42-45] There are three shorter and three longer Ag–O bond lengths within the AgO_6 units in $AgRuO_3$ (Figure 2a). A comparison of the Ag–O bond length in *R*-3 $AgBO_3$ is shown in Figure 2b, where the Ag–O distance in $AgRuO_3$ is obviously shorter than those in $AgBiO_3$ and $AgSbO_3$. Generally, shorter Ag–O bond lengths mean higher oxidation states of Ag considering its ionic radius (1.15, 0.79, and 0.75 Å for Ag^+, Ag^{2+}, and Ag^{3+}, respectively, in octahedral coordination) at different valence states.[46] The bond valence sum (BVS) calculations of Ag give somewhat larger values in $AgRuO_3$ than those in $AgSbO_3$ and $AgBiO_3$ (Figure 2b). Considering the shorter distance between Ag-Ru (3.174(1) Å) within the face-shared octahedral pairs, the higher oxidation state Ag ion could be ascribed to non-negligible covalent

Citation: *CCS Chem.* **2022**, Just Published. DOI: 10.31635/ccschem.022.202201989
Link to VoR: https://doi.org/10.31635/ccschem.022.202201989

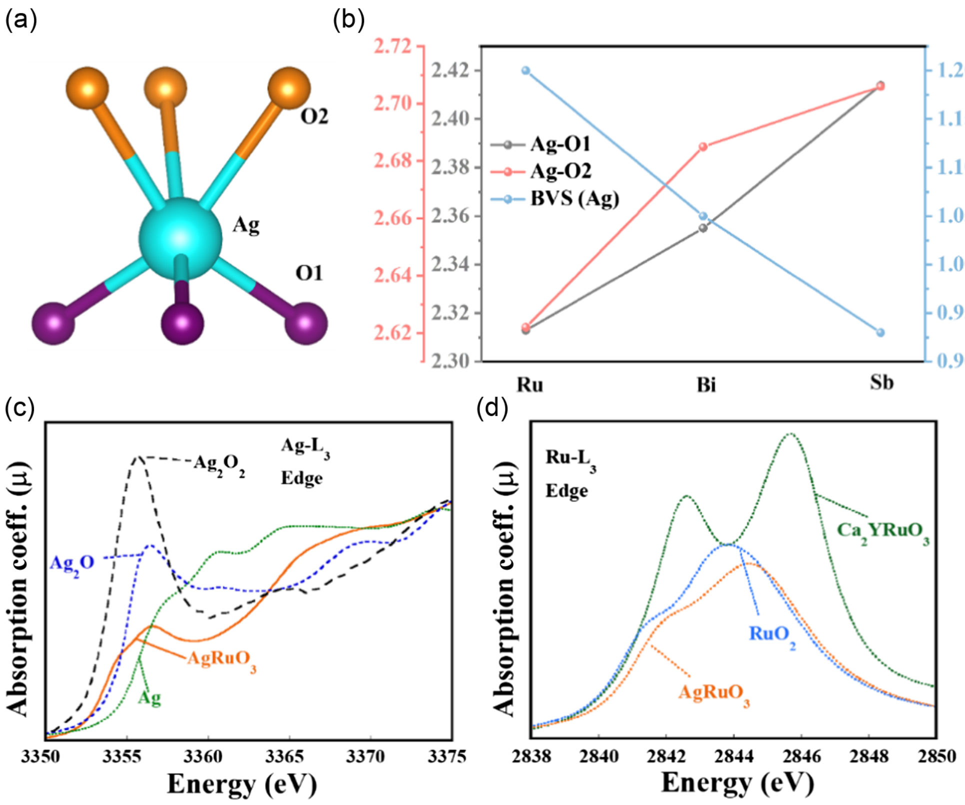

Figure 2 | *Local environment and electronic structure. (a) The distorted AgO_6 octahedron in $AgRuO_3$ at AP. (b) Comparison of the Ag–O bond length and corresponding BVS of Ag in $AgBO_3$* (B = Ru, Bi, Sb) *at AP and room temperature; XANES of $AgRuO_3$ for (c) Ag-L_3 edge and (d) Ru-L_3 edge.*

bonding nature as the case in fluorides, or charge disproportion between Ag and Ru, which, together with the long distance (5.406 Å) between the honeycomb RuO_6 layers, endows remarkable 2D features of $AgRuO_3$.

XANES data were further analyzed to confirm the oxidation state of cations. As displayed in Figure 2c, Ag L_3-edge XANES clearly reflects an emerged peak located at higher energy in $AgRuO_3$ compared with Ag^+ in Ag_2O, which is also distinct with Ag^+ and Ag^{3+} in AgO (Ag_2O_2). Since the nominal oxidation state of Ru in $AgRuO_3$ is between Ru^{4+} and Ru^{5+} referenced to $Ru^{4+}O_2$ and $Ca_2YRu^{5+}O_6$ (Figure 2d), the charged nominal formula of the title compound can be thus written as $Ag^{+1/+2}Ru^{+4/+5}O_3$. The mixed-valence case could also be found in the lighter homologue of Ag, such as the Cu^{1+}/Cu^{2+} ions in Cu_2IrO_3.[16] The electronic structure and valence state are also manifested by the magnetic properties, which are strongly related to the electronic configuration and exchange interactions. Ag_2O, Ag_2O_3, and AgO are diamagnetic, which is expected for Ag^+ (d^{10}) and square-planar Ag^{3+} (d^8) ions. Distinctly, the d^9-Ag^{2+} could endow interesting magnetic properties, such as a one-dimensional chain of Ag^{2+} ions with strong AFM coupling in $AgSO_4$ and a 2D AFM square net of Ag^{2+} ions in $Ag(pyz)_2(S_2O_8)$ (pyz = pyrazine).[47,48] Compared with the discoveries in literature, the inconsistency of crystal and electronic structure motivated us to reexamine the magnetism of the as-made $AgRuO_3$.[30,31] The temperature-dependent magnetic susceptibility of polycrystalline $AgRuO_3$ is nearly identical to that reported in literature, as shown in Supporting Information Figure S5. A sharp AFM transition is observed around 340 K in the FC curve at 0.1 T. The bifurcation of ZFC and FC curves appears upon cooling at 0.1 T below the AFM transition point. The magnetic susceptibility value is less magnetic field-dependent above 1 T and keeps decreasing upon cooling to 75 K, which is then followed by upturns in the $\chi(T)$ curves. At 7 T, the ZFC and FC curves nearly overlap. The presence of magnetic Ag^{2+} ions and interactions between Ag^{2+} and $Ru^{4+/5+}$ could be responsible for the bump around 50 K and transition around 120 K in the 0.1 T-ZFC $\chi(T)$ curve in Supporting Information Figure S5a. Besides, these magnetic transitions in the 0.1 T curves are strongly dependent on the applied field and highly suppressed at higher magnetic field, suggesting complicated magnetic phase transitions. The magnetic-field dependent $C_p(T)$ curves (Supporting Information Figure S5b) were measured on a pellet (cold pressed at 3 GPa using the polycrystalline powder). The low-temperature $C_p(T)$ data can be appropriately fitted by $C_p(T) = \gamma' T + \beta T^3 + \delta T^5$

Citation: *CCS Chem.* **2022**, Just Published. DOI: 10.31635/ccschem.022.202201989
Link to VoR: https://doi.org/10.31635/ccschem.022.202201989

($C_p/T - T^2$ plots in inset of Supporting Information Figures S5b), resulting in $\gamma' = 5.1(6)$ mJ mol^{-1} K^{-2}, $\beta = 0.885(1)$ mJ mol^{-1} K^{-4}, and $\delta = -0.00048(1)$ mJ mol^{-1} K^{-6}, which are very comparable to those reported by Jansen et al.[30] Taken together, the electronic structure of Ag and Ru is mixed d^9/d^{10} and d^3/d^4, respectively, in $AgRuO_3$.

Temperature- and pressure-dependent resistance results

Pressure is a unique thermodynamic variable to explore the phase transitions and novel physical phenomena inaccessible at ambient conditions.[49,50] The resistance (R) of polycrystalline $AgRuO_3$ was measured by a four-probe method in a DAC between 3 and 300 K up to 36 GPa (Supporting Information Figure S6). As shown in Figure 3a, the temperature-dependent $R(T)$ at 2.6 GPa exhibits a semiconducting behavior, similar to that at AP in literature.[30] $R(T)$ monotonically decreases nearly four orders of magnitude as the pressure increased from 2.6 to 3.0 and then to 4.5 GPa. Although the $R(T)$ at 3.0 and 4.5 GPa retains a semiconducting behavior, it becomes almost temperature-independent and close to the IMT boundary. Metallization appears from 4.5 to 8.7 GPa above 50 K, where $R(T)$ initially decreases upon cooling and reaches a plateau between 50 and 30 K, followed by an upturn to semiconducting behavior at lower temperatures (Figure 3b). Similar metallic-to-semiconducting transitions were maintained at 12.3 GPa but showed lower R values and less temperature dependence. At 16.1 GPa, $R(T)$ is slightly increased and becomes completely temperature-independent, approaching an unexpected crossover of MIT. The $R(T)$ plots become upward warping in the whole temperature region upon cooling at incremental pressures ranging between 22.1 and 36.3 GPa, where the upturns with steeper slopes are observed below ~20 K (Figure 3c). The overall R reaches a minimum (0.43 Ω) at 27.8 GPa, except the crossover with the 22.1 GPa plot below 75 K, where the R values of 22.1 GPa is slightly lower. At 36.3 GPa, R increases more rapidly upon cooling below 250 K. The R evolution can be more intuitively reflected by the P-T heat map in Supporting Information Figure S7.

The overall pressure- and temperature-dependent phase diagram of R is shown in Figure 3d. $AgRuO_3$ undergoes a sequential IMT and MIT transition when pressing up to 8.7 and 22.1 GPa, respectively. It is commonly believed that the metallic state is favored at high pressures, where the pressure-induced IMT in $AgRuO_3$ can be roughly attributed to enhanced band overlapping from lattice

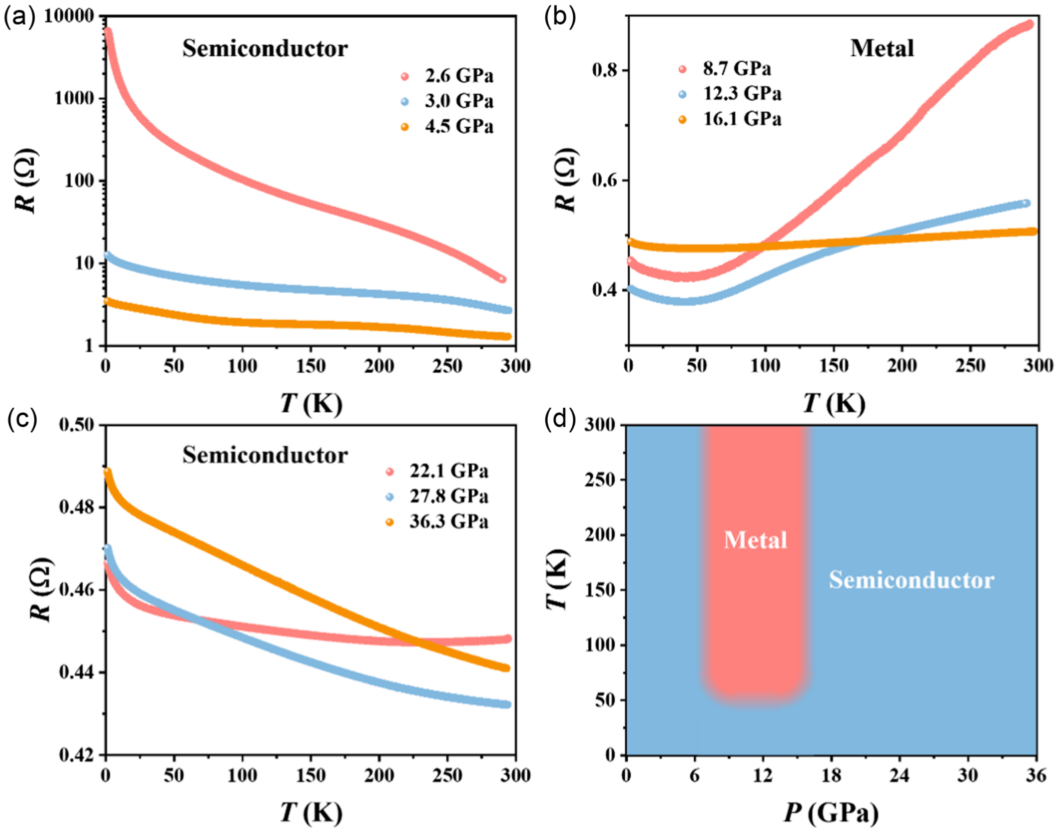

Figure 3 | *Pressure dependent resistance variation between 3 and 300 K. (a–c) Pressure dependent* R *variation plots of* $AgRuO_3$ *up to 36.3 GPa. (d) Pressure- and temperature-dependent heat map of* R *evolution of* $AgRuO_3$*.*

Citation: *CCS Chem.* **2022**, Just Published. DOI: 10.31635/ccschem.022.202201989
Link to VoR: https://doi.org/10.31635/ccschem.022.202201989

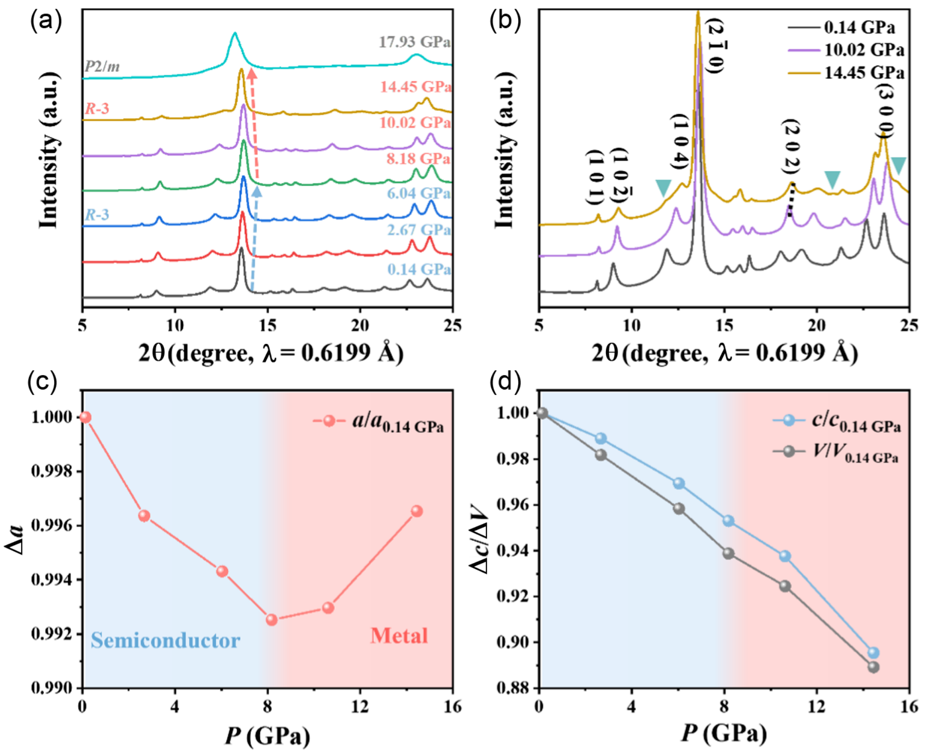

Figure 4 | *Pressure-induced structural evolution. (a) In-situ variable pressure SPXRD patterns collected at various pressures for $AgRuO_3$ upon pressing, the colored dash-line arrows highlight the peak evolution upon pressing. (b) SPXRD patterns at selected pressure to illustrate the peak shift, and the azury rectangles at 14.45 GPa mark the new peaks. (c and d) Pressure dependences of the lattice parameters.*

shrinkage.[51–53] Nevertheless, pressure-induced MIT has also been discovered in several quantum materials, since enhanced structural distortion can weaken the electron hopping and lead to localization in an insulating state.[54–56] The cell dimension keeps changing at increasing pressure, so it is impossible to generate the exact shape factor and thus, resistivity, for the detailed simulation of the conduction mechanism. Further, the upturns at lower temperatures need further investigation. The pressure-dependent isothermal $R(P)$ curves are displayed in Supporting Information Figure S8. At high temperatures, R decreases with increasing pressure, while at low temperatures, R drops to a minimum around 12.5 GPa, and then starts to rise until ~16 GPa, followed by less pressure-dependent concave curves at higher pressure. To correlate the pressure-dependent R evolution and structural modification in $AgRuO_3$, in-situ pressure-dependent SPXRD and Raman spectra were conducted at room temperature with smaller pressure intervals.

Pressure-induced intermetallic charge transfer

To assess the origin of the successive IMT-MIT in $AgRuO_3$, in situ pressure-dependent SPXRD patterns were collected at room temperature under various pressures to study the detailed structural modification (Figure 4a). The SPXRD pattern at 0.14 GPa can be well fitted by the ambient-pressure rhombohedral R-3 structure regardless of the absent peaks due to preferred orientation. Interestingly, as displayed in Figure 4b, anisotropic peak shifting is observed in the intermediate pressure (metallic) region, which is distinct to the cases at lower pressures. Up to 14.45 GPa, extra peaks appear in the patterns, indicating the emergence of pressure-induced structural phase transition. Remarkably, these structural changes are consistent with the successive MIT in the $AgRuO_3$. Figures 4c and 4d display the pressure dependence of normalized lattice parameters deduced from Le Bail fit of the SPXRD patterns. Apparently, anisotropic compressibility arises in $AgRuO_3$. As expected, the c-axis contracts with increasing pressure, indicating a narrowing of the interplanar distance. In contrast, the ab-plane exhibits robust anti-compressibility with negligible changes and an abnormal negative compressibility is observed in the pressure region where metallic behavior is observed, indicating that the structural modulation has a profound impact on the electrical transport property.

Due to angular constraints and background from the DAC environment, the detailed crystallographic information cannot be decently refined from the SPXRD data. Combined with the deduced lattice parameters,

Citation: *CCS Chem.* **2022**, Just Published. DOI: 10.31635/ccschem.022.202201989
Link to VoR: https://doi.org/10.31635/ccschem.022.202201989

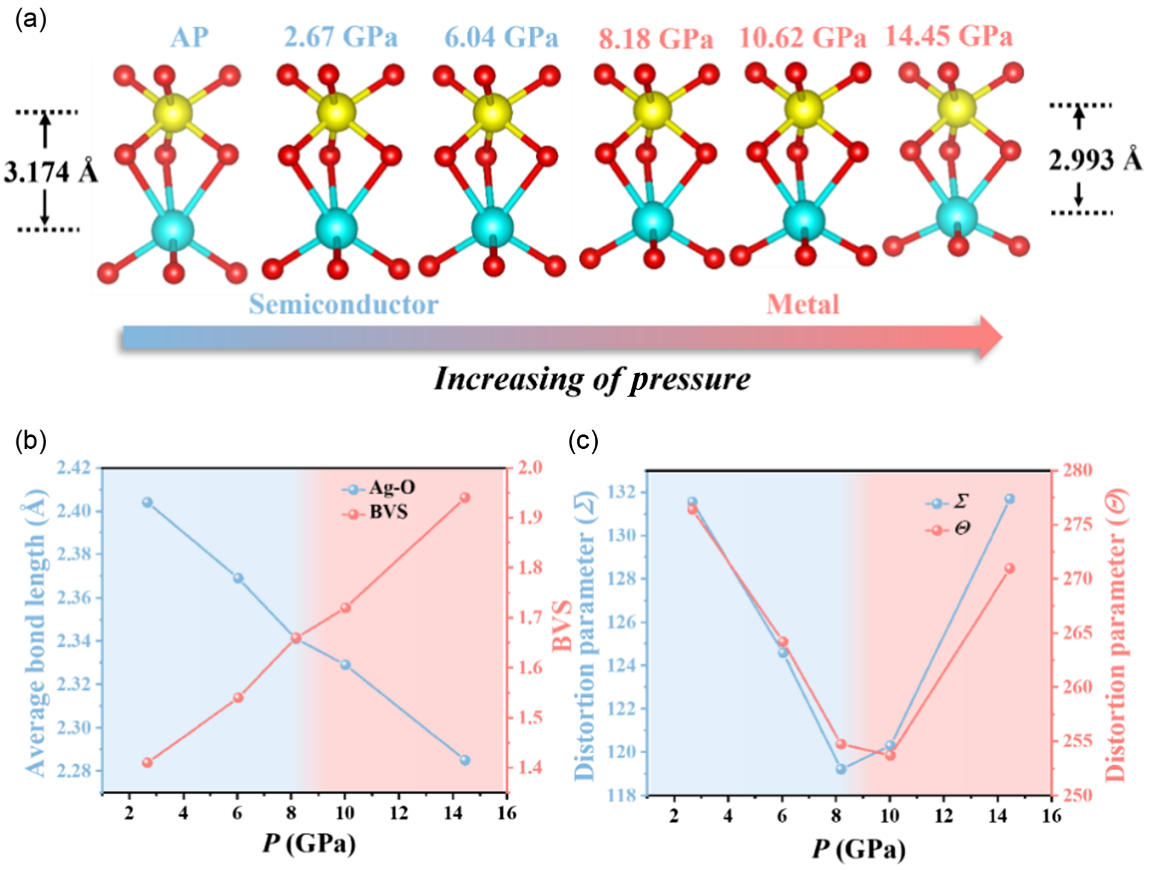

Figure 5 | *Pressure-dependent local structure variation. (a) Schematic illustrations with respect to face-sharing RuO_6 and AgO_6 octahedra of $AgRuO_3$ refined from in-situ variable pressure SPXRD. (b) Bond length and corresponding BVS of AgO_6 octahedra. (c) AgO_6 octahedron distortion (Σ and Θ) of $AgRuO_3$.*

CALYPSO search provides reasonable crystal information for the pressure range of the first IMT. Figure 5a displays the calculated pressure-dependent local structural evolution of the face-shared octahedral pair in the *R*-3 zone, where the Ag-Ru distance decreases with shrinkage along the *c*-axis, from 3.174 Å at AP to 2.993 Å at 14.45 GPa, which is indicative of strong orbital overlap between Ru and Ag. The shorter Ag–Ru bond length endows stronger electrostatic repulsive forces between the face-sharing pairs. To minimize the repulsion, octahedral distortion plays a vital role.[57] The Ag atom becomes displaces and off center in the face-sharing octahedral dimer, while Ru slightly displaces away from the octahedral centroid, inducing drastic distortions of the AgO_6 ligand octahedron. The displacement of Ag promotes charge transfer between Ag and Ru through the bridged O triangle of the shared face.[58] To aid this case, the charge distribution in $AgRuO_3$ under elevated pressure was investigated using BVS determined from calculated structural information (Supporting Information Tables S4 and S5). Corresponding selected inter atomic distances, BVS, and octahedral distortion parameters are shown in Figure 5b, where Σ and Θ are the sum of the deviation of 6 and 24 unique θ angles in the octahedra, respectively.[59,60] Due to the similar ionic sizes of Ru^{4+} and Ru^{5+}, the Ru–O bond lengths display a slight change upon pressing (Supporting Information Figure S9). Thus, the oxidation state of Ag was used to identify the charge redistribution for $AgRuO_3$. As mentioned above, the BVS at AP confirm the $Ag^{+1/+2}Ru^{+4/+5}O_3$ distribution, in which that of Ag is close to 1.2. With the elevated pressure, a successive charge transfer is ignited in this system. A drastic change is observed above 6 GPa, where the BVS for Ag is larger than 1.5, indicating Ag^{2+} domination at higher pressure. Further incremental pressure increases resulted in the formation of an almost completed Ag^{2+} site, where the whole Ag^{2+} dominant range demonstrated unusual metallic behavior, which is consistent with the observed IMT in $AgRuO_3$ (Figure 3).

Domination of Ag^{2+} in $AgRuO_3$ gives rise to charge redistribution, leading to phase transition to a new HP phase. Substantial peak broadening above 17.92 GPa hinders possible identification of the structural symmetry, thus the emergent semi-conductive phase above 17.93 GPa was not experimentally investigated further in this study. Subsequent diffraction peak indexation and CALYPSO screening yielded a possible phase with space

Citation: *CCS Chem.* **2022**, Just Published. DOI: 10.31635/ccschem.022.202201989
Link to VoR: https://doi.org/10.31635/ccschem.022.202201989

group of $P2/m$ above 17.93 GPa, where the AgO_4 square-planar and RuO_6 octahedral pairs are aligned along the *c*-axis (Supporting Information Figure S10 and Tables S6 and S7). The BVS calculations of Ag give larger values than that at AP, indicating a higher oxidation state in this HP phase. To date, five binary silver oxides have been studied and structurally characterized, and the corresponding bond length and BVS calculations are listed in Supporting Information Table S8 for comparison, where Ag_6O_2 is not included. AgO is not a Ag^{2+} compound but reported to be diamagnetic mixed-valence as $Ag^{+}Ag^{3+}O_2$, where Ag_2O_3 contains only Ag^{3+} ions, while Ag_3O_4 is also a mixed-valent oxide as $(Ag^{2.67+})_3O_4$ with no evidence of Ag^{2+} cations.[61–64] Considering the observed bond length and BVS calculations of Ag, the HP $P2/m$-$AgRuO_3$ displays comparable bond lengths with $AgSO_4$, dedicating new charge-ordering with unusual Ag^{2+}. In addition, the calculated density of state (DOS) presents a typical metallic behavior, which is, however, inconsistent with experimental observations. This anomaly could be ascribed the enhanced structural distortion under high pressure, which can weaken the electron hopping and lead to localization in an insulating state.[54–56]

Ag^{2+} is isoelectronic with Cu^{2+} (d^9), so elongated Jahn-Teller distortion would be ignited in Ag^{2+}-dominated AgO_6 octahedra. Thus, the compressibility of the *ab*-plane relies on the pressure-induced contraction and equatorial elongation of the $Ag^{2+}O_6$ octahedra. When it comes into the Ag^{2+}-dominant range, the elongation effect overwhelms that of pressure, leading to an abnormally negative compressibility. This case could be revealed by the octahedral distortion parameters (Figure 5c), where the larger octahedral distortion means the stronger equatorial elongation of the octahedra due to Jahn-Teller distortion in this case, leading to poor compressibility of the *ab*-plane. This could be also an indicator of the existence of unusual Ag^{2+}. Raman spectroscopy is also an effective and powerful tool in detecting lattice vibrations, which can tell the electron-phonon coupling, weak lattice distortion, and/or structural transition. Supporting Information Figure S11 shows the pressure-dependent Raman spectroscopy on polycrystalline $AgRuO_3$ between 100–700 cm^{-1}, up to 20.20 GPa. The data below 150 cm^{-1} shows a poor signal to noise ratio, which are not further considered in this study. According to a previous study, selected modes are also displayed in Supporting Information Figure S12.[30] Distinctly, the Raman shift trend can be sorted to three pressure regions between 1.07–5.01 GPa, 7.97–14.58 GPa, and 15.80–20.20 GPa, respectively, which are also in accordance with the continuous IMT and MIT transitions. In the first two pressure zones, most mode peaks exhibit a linear shift under pressure, while the pressure-induced shift around 482 cm^{-1} is markedly lower than those of other peaks. This difference is likely due to the pressure-induced charge transfer between Ag and Ru, associated with anomalously negative compressibility in the *ab*-plane with reduced stretching modes. Above 15.80 GPa, the signals not only display the appearance of new peaks, but also become significantly broader, likely showcasing a structural transition with the amorphous state under high pressure. Taken together, the face-sharing AgO_6 and RuO_6 octahedra between the honeycomb layer triggers the exchange interaction through the bridged oxygen under applied pressure and enables the charge transfer and thus the valence redistribution for both Ag and Ru, which endows the unusual Ag^{2+} domination with the metallic state in the honeycomb lattice.

DFT calculations

To further understand the charge redistribution in $AgRuO_3$ with elevated pressure, DFT calculations were performed to differentiate the crystal structures with anisotropic expansion. Distinctly, the electron localization function (ELF) displayed in Figures 6a and 6b revealed an increasing partial charge density for the Ru atom, where the charge accumulated at the surface with elevated pressure. This can be clearly observed in the ELF maps for the Ru honeycomb lattice, in which the accumulated charge on the Ru atom signifies the pressure-induced charge transfer. This is consistent with the Bader charge analysis (Supporting Information Table S9), from which the charge transferred from Ag to the Ru atoms, leading to the unusual Ag^{2+} in the honeycomb lattice. The calculations based on periodic boundary conditions show that an AFM state is energetically favorable for both the *R*-3 and $P2/m$ polymorphs, which is in good agreement with the experimentally evidenced magnetic ground state.[31] The band gap around the Fermi level (E_F) displays a dramatic contraction with applied pressure (0.05 eV at 10.02 GPa vs 0.36 eV at AP), confirming that the MIT is ignited by pressure in $AgRuO_3$ (Figures 6c and 6d). While a negligible band gap still exists at 10.02 GPa in this system, this may be due to the fact that DFT underestimates the electronic correlations in the correlated systems. Here the pressure-induced intermetallic charge transition in $AgRuO_3$ with the occurrence of MIT transition, especially the unprecedented discovery of pressure-tuned Ag^{2+} in oxide, will invite more solid studies in the future.

Conclusions

We have shown that the as-made $AgRuO_3$ adopts the typical ilmenite structure (*R*-3) other than the reported *c*-axis doubled super-cell (*R*-3*c*). Reproducible SCXRDs, SPXRD, and XANES indicate the *R*-3 nominal structure as $Ag^{+1/+2}Ru^{+4/+5}O_3$. It undergoes a pressure-induced successive insulator-metal-insulator transition ignited in

Citation: *CCS Chem.* **2022**, Just Published. DOI: 10.31635/ccschem.022.202201989
Link to VoR: https://doi.org/10.31635/ccschem.022.202201989

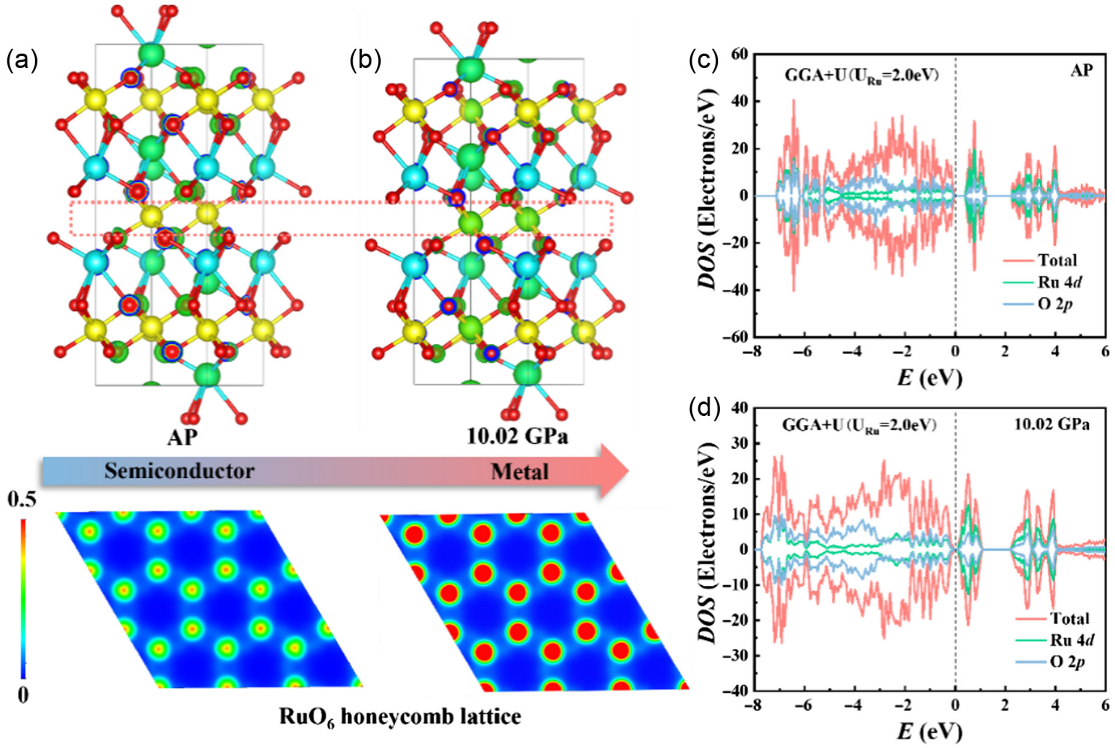

Figure 6 | *(a and b) Calculated ELF for $AgRuO_3$ at AP and 10.02 GPa, respectively. The green color around the atom is denoted as charge distribution. The corresponding ELF maps for the RuO_6 honeycomb lattice are showed on the bottom. (c and d) The DOS of $AgRuO_3$ under AP and 10.02 GPa, respectively.*

the honeycomb lattice. Bond valence analyses and electronic structure calculations based on in situ HP SPXRD reveal an unprecedented simultaneous charge transfer between Ag and Ru, accompanied by a metallic behavior gradually changing from Ag^{1+}/Ru^{5+} to Ag^{2+}/Ru^{4+} domination, and negative compressibility in the *ab*-plane in the *R*-3 phase between 8.18 and 14.45 GPa upon pressing. Further structural transition to *P*2/*m* at higher pressure was also predicted. This study demonstrates the significant role in understanding the charge state, especially for charge distribution in Ag oxides, which will accordingly drive many preternatural phenomena.

Supporting Information

Supporting Information is available and includes TGA, in-situ VT/VP-PXRD, magnetic properties, specific heat, pressure-dependent Raman spectra, and crystallographic parameters of $AgRuO_3$. The supporting crystallographic information file may also be obtained from FIZ Karlsruhe, 76344 Eggenstein-Leopoldshafen, Germany (e-mail: crysdata@fiz-karlsruhe.de), on quoting the deposition number CSD-2157087 (293 k), CSD-2157086 (150 K), and CSD-2157085 (100 K). Crystallographic information file (cif) for $AgRuO_3$-293 K, $AgRuO_3$-150 K, and $AgRuO_3$-100 K.

Conflict of Interest

There is no conflict of interest to report.

Funding Information

This work was financially supported by the National Science Foundation of China (grant nos. NSFC-22090041, 21875287, U1932217, 11974246, 12004252, 12025408, 11921004, 11974432, and 92165204), the Program for Guangdong Introducing Innovative and Entrepreneurial Teams (grant no. 2017ZT07C069), NKRDPC-2017YFA0206203, NKRDPC-2018YFA0306001.

Acknowledgments

The XANES were performed by Conan Weiland (National Institute of Standards and Technology) on NSLS-II beamline 7-ID-2 SST-2 and supported in part under Department of Energy/Basic Energy Sciences (DE-SC0012704). The authors thank the National Supercomputer Center in Guangzhou, and the staffs from BL14B and BL15U1 at SSRF for assistance during data collection.

References

1. Zhang, L.; Wang, Y.; Lv, J.; Ma, Y. Materials Discovery at High Pressures. *Nat. Rev. Mater.* **2017**, *2*, 17005.

Citation: *CCS Chem.* **2022**, Just Published. DOI: 10.31635/ccschem.022.202201989
Link to VoR: https://doi.org/10.31635/ccschem.022.202201989

2. Xu, M.; Li, Y.; Ma, Y. Materials by Design at High Pressures. *Chem. Sci.* **2022**, *13*, 329–344.

3. Jiang, D.; Wen, T.; Song, H.; Jiang, Z.; Li, C.; Liu, K.; Yang, W.; Mao, H.; Wang, Y. Intrinsic Zero-Linear and Zero-Area Compressibilities over an Ultrawide Pressure Range within a Gear-Spring Structure. *CCS Chem.* **2022**. DOI: https://doi.org/10.31635/ccschem.022.202101739

4. Li, M. R.; Adem, U.; McMitchell, S. R.; Xu, Z.; Thomas, C. I.; Warren, J. E.; Giap, D. V.; Niu, H.; Wan, X.; Palgrave, R. G.; Schiffmann, F.; Cora, F.; Slater, B.; Burnett, T. L.; Cain, M. G.; Abakumov, A. M.; van Tendeloo, G.; Thomas, M. F.; Rosseinsky, M. J.; Claridge, J. B. A Polar Corundum Oxide Displaying Weak Ferromagnetism at Room Temperature. *J. Am. Chem. Soc.* **2012**, *134*, 3737–3747.

5. Ju, S.; Cai, T. Y.; Lu, H. S.; Gong, C. D. Pressure-Induced Crystal Structure and Spin-State Transitions in Magnetite (Fe_3O_4). *J. Am. Chem. Soc.* **2012**, *134*, 13780–13786.

6. Chen, X. J.; Struzhkin, V. V.; Yu, Y.; Goncharov, A. F.; Lin, C. T.; Mao, H. K.; Hemley, R. J. Enhancement of Superconductivity by Pressure-Driven Competition in Electronic Order. *Nature* **2010**, *466*, 950–953.

7. Azuma, M.; Carlsson, S.; Rodgers, J.; Tucker, M. G.; Tsujimoto, M.; Ishiwata, S.; Isoda, S.; Shimakawa, Y.; Takano, M.; Attfield, J. P. Pressure-Induced Intermetallic Valence Transition in $BiNiO_3$. *J. Am. Chem. Soc.* **2007**, *129*, 14433–14436.

8. Seda, T.; Hearne, G. R. Pressure Induced $Fe^{2+}+Ti^{4+} \rightarrow Fe^{3+}+Ti^{3+}$ Intervalence Charge Transfer and the Fe^{3+}/Fe^{2+} Ratio in Natural Ilmenite $FeTiO_3$ Minerals. *J. Phys.: Condens. Mat.* **2004**, *16*, 2707–2718.

9. Hosaka, Y.; Denis Romero, F.; Ichikawa, N.; Saito, T.; Shimakawa, Y. Successive Charge Transitions of Unusually High-Valence $Fe^{3.5+}$: Charge Disproportionation and Intermetallic Charge Transfer. *Angew. Chem. Int. Ed.* **2017**, *56*, 4243–4246.

10. Long, Y. W.; Hayashi, N.; Saito, T.; Azuma, M.; Muranaka, S.; Shimakawa, Y. Temperature-Induced A-B Intersite Charge Transfer in an A-Site-Ordered $LaCu_3Fe_4O_{12}$ Perovskite. *Nature* **2009**, *458*, 60–63.

11. Cohen, N.; Diéguez, O. Two Types of Charge Ordering in Bismuth Nickelate. *Phys. Rev. B* **2021**, *104*, 064111.

12. Wang, X.; Liu, Z.; Ye, X.; Zhou, B.; Hu, Z.; Wang, W.; Yu, R.; Agrestini, S.; Zhou, G.; Chen, K.; Choueikani, F.; Ohresser, P.; Baudelet, F.; Lin, H. J.; Chen, C. T.; Tanaka, A.; Weng, S. C.; Long, Y. Os Doping Suppressed Cu-Fe Charge Transfer and Induced Structural and Magnetic Phase Transitions in $LaCu_3Fe_{4\text{-}x}Os_xO_{12}$ (x = 1 and 2). *Inorg. Chem.* **2021**, *60*, 6298–6305.

13. Rezaei, N.; Hansmann, P.; Bahramy, M. S.; Arita, R. Mechanism of Charge Transfer/Disproportionation in $Ln\mathrm{Cu_3Fe_4O_{12}}$ (Ln = lanthanides). *Phys. Rev. B* **2014**, *89*, 125125.

14. Etani, H.; Yamada, I.; Ohgushi, K.; Hayashi, N.; Kusano, Y.; Mizumaki, M.; Kim, J.; Tsuji, N.; Takahashi, R.; Nishiyama, N.; Inoue, T.; Irifune, T.; Takano, M. Suppression of Intersite Charge Transfer in Charge-Disproportionated Perovskite $YCu_3Fe_4O_{12}$. *J. Am. Chem. Soc.* **2013**, *135*, 6100–6106.

15. Blanchard, P. E.; Chapman, K. W.; Heald, S. M.; Zbiri, M.; Johnson, M. R.; Kennedy, B. J.; Ling, C. D. Direct Observation of Pressure-Driven Valence Electron Transfer in $Ba_3BiRu_2O_9$, $Ba_3BiIr_2O_9$, and $Ba_4BiIr_3O_{12}$. *Inorg. Chem.* **2016**, *55*, 5649–5654.

16. Abramchuk, M.; Ozsoy-Keskinbora, C.; Krizan, J. W.; Metz, K. R.; Bell, D. C.; Tafti, F. Cu_2IrO_3: A New Magnetically Frustrated Honeycomb Iridate. *J. Am. Chem. Soc.* **2017**, *139*, 15371–15376.

17. Cava, R. J. Schizophrenic Electrons in Ruthenium-Based Oxides. *Dalton Trans.* **2004**, 2979–2987.

18. Denis Romero, F.; Burr, S. J.; McGrady, J. E.; Gianolio, D.; Cibin, G.; Hayward, M. A. $SrFe_{0.5}Ru_{0.5}O_2$: Square-Planar Ru^{2+} in an Extended Oxide. *J. Am. Chem. Soc.* **2013**, *135*, 1838–1844.

19. Streltsov, S. V. Low-Dimensional Ruthenates with Honeycomb Lattice. *Phys. Met. Metallogr.* **2019**, *119*, 1276–1279.

20. Hiley, C. I.; Lees, M. R.; Fisher, J. M.; Thompsett, D.; Agrestini, S.; Smith, R. I.; Walton, R. I. Ruthenium(V) Oxides from Low-Temperature Hydrothermal Synthesis. *Angew. Chem. Int. Ed.* **2014**, *53*, 4423–4427.

21. Suzuki, H.; Gretarsson, H.; Ishikawa, H.; Ueda, K.; Yang, Z.; Liu, H.; Kim, H.; Kukusta, D.; Yaresko, A.; Minola, M.; Sears, J. A.; Francoual, S.; Wille, H. C.; Nuss, J.; Takagi, H.; Kim, B. J.; Khaliullin, G.; Yavas, H.; Keimer, B. Spin Waves and Spin-State Transitions in a Ruthenate High-Temperature Antiferromagnet. *Nat. Mater.* **2019**, *18*, 563–567.

22. Park, J.; Tan, T. Y.; Adroja, D. T.; Daoud-Aladine, A.; Choi, S.; Cho, D. Y.; Lee, S. H.; Kim, J.; Sim, H.; Morioka, T.; Nojiri, H.; Krishnamurthy, V. V.; Manuel, P.; Lees, M. R.; Streltsov, S. V.; Khomskii, D. I.; Park, J. G. Robust Singlet Dimers with Fragile Ordering in Two-Dimensional Honeycomb Lattice of Li_2RuO_3. *Sci. Rep.* **2016**, *6*, 25238.

23. Kimber, S. A. J.; Mazin, I. I.; Shen, J.; Jeschke, H. O.; Streltsov, S. V.; Argyriou, D. N.; Valentí, R.; Khomskii, D. I. Valence Bond Liquid Phase in the Honeycomb Lattice Material Li_2RuO_3. *Phys. Rev. B* **2014**, *89*, 081408.

24. Huang, B.; Liu, Z.; Han, Y.; Zhao, S.; Wu, M.; Frank, C. E.; Greenblatt, M.; Croft, M.; Quackenbush, N. F.; Liu, S.; Tyson, T. A.; Zhang, L.; Sun, J.; Shan, P.; Dai, J.; Yu, X.; Cheng, J.; Li, M. R. Nonmetallic Metal toward a Pressure-Induced Bad-Metal State in Two-Dimensional $Cu_3LiRu_2O_6$. *Chem. Commun.* **2019**, *56*, 265–268.

25. Banerjee, A.; Yan, J.; Knolle, J.; Bridges, C. A.; Stone, M. B.; Lumsden, M. D.; Mandrus, D. G.; Tennant, D. A.; Moessner, R.; Nagler, S. E. Neutron Scattering in the Proximate Quantum Spin Liquid α-$RuCl_3$. *Science* **2017**, *356*, 1055–1059.

26. Laurell, P.; Okamoto, S. Dynamical and Thermal Magnetic Properties of the Kitaev Spin Liquid Candidate α-$RuCl_3$. *NPJ Quantum Mater.* **2020**, *5*, 2.

27. Wang, Z.; Reschke, S.; Huvonen, D.; Do, S. H.; Choi, K. Y.; Gensch, M.; Nagel, U.; Room, T.; Loidl, A. Magnetic Excitations and Continuum of a Possibly Field-Induced Quantum Spin Liquid in α-$RuCl_3$. *Phys. Rev. Lett.* **2017**, *119*, 227202.

28. Broholm, C.; Cava, R. J.; Kivelson, S. A.; Nocera, D. G.; Norman, M. R.; Senthil, T. Quantum Spin Liquids. *Science* **2020**, *367*, eaay0668.

29. Chamorro, J. R.; McQueen, T. M.; Tran, T. T. Chemistry of Quantum Spin Liquids. *Chem. Rev.* **2021**, *121*, 2898–2934.

30. Schnelle, W.; Prasad, B. E.; Felser, C.; Jansen, M.; Komleva, E. V.; Streltsov, S. V.; Mazin, I. I.; Khalyavin, D.;

Manuel, P.; Pal, S.; Muthu, D. V. S.; Sood, A. K.; Klyushina, E. S.; Lake, B.; Orain, J.-C.; Luetkens, H. Magnetic and Electronic Ordering Phenomena in the Ru_2O_6-Layer Honeycomb Lattice Compound $AgRuO_3$. *Phys. Rev. B* **2021**, *103*, 214413.

31. Prasad, B. E.; Kanungo, S.; Jansen, M.; Komarek, A. C.; Yan, B.; Manuel, P.; Felser, C. $AgRuO_3$, a Strongly Exchange-Coupled Honeycomb Compound Lacking Long-Range Magnetic Order. *Chem.-Eur. J.* **2017**, *23*, 4680–4686.

32. Coelho, A. TOPAS and TOPAS-Academic: An Optimization Program Integrating Computer Algebra and Crystallographic Objects Written in C++. *J. Appl. Crystallogr.* **2018**, *51*, 210–218.

33. Dolomanov, O. V.; Bourhis, L. J.; Gildea, R. J.; Howard, J. A. K.; Puschmann, H. OLEX2: A Complete Structure Solution, Refinement and Analysis Program. *J. Appl. Crystallogr.* **2009**, *42*, 339–341.

34. Wang, Y.; Lv, J.; Zhu, L.; Ma, Y. Crystal Structure Prediction via Particle-Swarm Optimization. *Phys. Rev. B* **2010**, *82*, 094116.

35. Wang, Y.; Lv, J.; Zhu, L.; Ma, Y. CALYPSO: A Method for Crystal Structure Prediction. *Comput. Phys. Commun.* **2012**, *183*, 2063–2070.

36. Gao, B.; Gao, P.; Lu, S.; Lv, J.; Wang, Y.; Ma, Y. Interface Structure Prediction via CALYPSO Method. *Sci. Bull.* **2019**, *64*, 301–309.

37. Blochl, P. E. Projector Augmented-Wave Method. *Phys. Rev. B* **1994**, *50*, 17953–17979.

38. Kresse, G.; Joubert, D. From Ultrasoft Pseudopotentials to the Projector Augmented-Wave Method. *Phys. Rev. B* **1999**, *59*, 1758–1775.

39. Kresse, G.; Furthmuller, J. Efficient Iterative Schemes for Ab Initio Total-Energy Calculations Using a Plane-Wave Basis Set. *Phys. Rev. B* **1996**, *54*, 11169–11186.

40. Perdew, J. P.; Burke, K.; Ernzerhof, M. Generalized Gradient Approximation Made Simple. *Phys. Rev. Lett.* **1996**, *77*, 3865–3868.

41. Liechtenstein, A. I.; Anisimov, V. V.; Zaanen, J. Density-Functional Theory and Strong Interactions: Orbital Ordering in Mott-Hubbard Insulators. *Phys. Rev. B* **1995**, *52*, R5467–R5470.

42. Farid, U.; Khan, H. U.; Avdeev, M.; Injac, S.; Kennedy, B. J. Structural Studies of the High Temperature Phases of $AgTaO_3$. *J. Solid State Chem.* **2018**, *258*, 859–864.

43. Sciau, P.; Kania, A.; Dkhil, B.; Suard, E.; Ratuszna, A. Structural Investigation of $AgNbO_3$ Phases Using X-Ray and Neutron Diffraction. *J. Phys.: Condens. Mat.* **2004**, *16*, 2795–2810.

44. Nalbandyan, V. B.; Avdeev, M.; Pospelov, A. A. Ion Exchange Reactions of $NaSbO_3$ and Morphotropic Series $MSbO_3$. *Solid State Sci.* **2006**, *8*, 1430–1437.

45. Kumada, N.; Kinomura, N.; Sleight, A. W. Neutron Powder Diffraction Refinement of Ilmenite-Type Bismuth Oxides: $ABiO_3$ (A = Na, Ag). *Mater. Res. Bull.* **2000**, *35*, 2397–2402.

46. Shannon, R. D. Revised Effective Ionic Radii and Systematic Studies of Interatomic Distances in Halides and Chalcogenides. *Acta Crystallogr. A* **1976**, *32*, 751–767.

47. Manson, J. L.; Stone, K. H.; Southerland, H. I.; Lancaster, T.; Steele, A. J.; Blundell, S. J.; Pratt, F. L.; Baker, P. J.; McDonald, R. D.; Sengupta, P.; Singleton, J.; Goddard, P. A.; Lee, C.; Whangbo, M. H.; Warter, M. M.; Mielke, C. H.; Stephens, P. W. Characterization of the Antiferromagnetism in $Ag(pyz)_2(S_2O_8)$ (pyz = pyrazine) with a Two-Dimensional Square Lattice of Ag^{2+} Ions. *J. Am. Chem. Soc.* **2009**, *131*, 4590–4591.

48. Kohler, J. Strong One-Dimensional Antiferromagnetic Interactions of Silver(II) Ions in Silver Sulfate. *Angew. Chem. Int. Ed.* **2010**, *49*, 3114–3115.

49. Ma, Z.; Li, F.; Zhao, D.; Xiao, G.; Zou, B. Whether or Not Emission of Cs_4PbBr_6 Nanocrystals: High-Pressure Experimental Evidence. *CCS Chem.* **2020**, *2*, 71–80.

50. Fang, Y.; Zhang, L.; Yu, Y.; Yang, X.; Wang, K.; Zou, B. Manipulating Emission Enhancement and Piezochromism in TwoDimensional Organic-Inorganic Halide Perovskite $[(HO)(CH_2)_2NH_3)]_2PbI_4$ by High Pressure. *CCS Chem.* **2020**, *2*, 2203–2210.

51. Oliva, R.; Laurien, M.; Dybala, F.; Kopaczek, J.; Qin, Y.; Tongay, S.; Rubel, O.; Kudrawiec, R. Pressure Dependence of Direct Optical Transitions in ReS_2 and $ReSe_2$. *NPJ 2D Mater. Appl.* **2019**, *3*, 20.

52. Zhao, Z.; Zhang, H.; Yuan, H.; Wang, S.; Lin, Y.; Zeng, Q.; Xu, G.; Liu, Z.; Solanki, G. K.; Patel, K. D.; Cui, Y.; Hwang, H. Y.; Mao, W. L. Pressure Induced Metallization with Absence of Structural Transition in Layered Molybdenum Diselenide. *Nat. Commun.* **2015**, *6*, 7312.

53. Yamamoto, T.; Zeng, D.; Kawakami, T.; Arcisauskaite, V.; Yata, K.; Patino, M. A.; Izumo, N.; McGrady, J. E.; Kageyama, H.; Hayward, M. A. The Role of Pi-Blocking Hydride Ligands in a Pressure-Induced Insulator-to-Metal Phase Transition in $SrVO_2H$. *Nat. Commun.* **2017**, *8*, 1217.

54. Chen, C.-H.; Zhou, Y.-H.; Zhou, Y.; Yuan, Y.-F.; An, C.; Chen, X.-L.; Tian, Z.-M.; Yang, Z.-R. Pressure-Induced Anomalous Insulating Behavior in Frustrated Iridate $La_3Ir_3O_{11}$. *Chin. Phys. B* **2021**, *30*, 067402.

55. Chen, C.; Zhou, Y.; Chen, X.; Han, T.; An, C.; Zhou, Y.; Yuan, Y.; Zhang, B.; Wang, S.; Zhang, R.; Zhang, L.; Zhang, C.; Yang, Z.; DeLong, L. E.; Cao, G. Persistent Insulating State at Megabar Pressures in Strongly Spin-Orbit Coupled Sr_2IrO_4. *Phys. Rev. B* **2020**, *101*, 144102.

56. Kusmartseva, A. F.; Sinclair, A.; Rodgers, J. A.; Kimber, S. A. J.; Attfield, J. P. Possible High-Pressure Orbital Quantum Criticality and an Emergent Resistive Phase in $PbRuO_3$. *Phys. Rev. B* **2013**, *87*, 165130.

57. Belik, A. A.; Matsushita, Y.; Katsuya, Y.; Tanaka, M.; Kolodiazhnyi, T.; Isobe, M.; Takayama-Muromachi, E. Crystal Structure and Magnetic Properties of 6*H*-$SrMnO_3$. *Phys. Rev. B* **2011**, *84*, 094438.

58. Søndenå, R.; Stølen, S.; Ravindran, P.; Grande, T.; Allan, N. L. Corner- versus Face-Sharing Octahedra in $AMnO_3$ Perovskites (A = Ca, Sr, and Ba). *Phys. Rev. B* **2007**, *75*, 184105.

59. Alonso, J. A.; Martinez-Lope, M. J.; Casais, M. T.; Fernandez-Daz, M. T. Evolution of the Jahn-Teller Distortion of MnO_6 Octahedra in $RMnO_3$ Perovskites (R = Pr, Nd, Dy, Tb,

Citation: *CCS Chem.* **2022**, Just Published. DOI: 10.31635/ccschem.022.202201989
Link to VoR: https://doi.org/10.31635/ccschem.022.202201989

Ho, Er, Y): A Neutron Diffraction Study. *Inorg. Chem.* **2000**, *39*, 917–923.

60. Buron-Le Cointe, M.; Hébert, J.; Baldé, C.; Moisan, N.; Toupet, L.; Guionneau, P.; Létard, J. F.; Freysz, E.; Cailleau, H.; Collet, E. Intermolecular Control of Thermoswitching and Photoswitching Phenomena in Two Spin-Crossover Polymorphs. *Phys. Rev. B* **2012**, *85*, 064114.

61. Quan, Y.; Pickett, W. E. Analysis of Charge States in the Mixed-Valent Ionic Insulator AgO. *Phys. Rev. B* **2015**, *91*, 035121.

62. McKeown, D. A.; Gan, H.; Pegg, I. L. Silver Valence and Local Environments in Borosilicate and Calcium Aluminoborate Waste Glasses as Determined from X-Ray Absorption Spectroscopy. *J. Non-Cryst. Solids* **2005**, *351*, 3826–3833.

63. Standke, B.; Jansen, M. Ag_3O_4, the First Silver(II,III) Oxide. *Angew. Chem. Int. Ed.* **1986**, *25*, 77–78.

64. Standke, B.; Jansen, M. Ag_2O_3, a Novel Binary Silver Oxide. *Angew. Chem. Int. Ed.* **1985**, *24*, 118–119.

Citation: *CCS Chem.* **2022**, Just Published. DOI: 10.31635/ccschem.022.202201989
Link to VoR: https://doi.org/10.31635/ccschem.022.202201989